Astron. Astrophys. 319, 737–746 (1997)

ASTRONOMY
AND
ASTROPHYSICS

Shocks and ring in the barred spiral galaxy NGC 1530

D. Reynaud and D. Downes

Institut de Radio Astronomie Millimétrique, F-38406 Saint Martin d'Hères, France

Received 8 July 1996 / Accepted 2 September 1996

Abstract. We present new CO(1–0) and HCN(1–0) observations of the barred spiral galaxy NGC 1530 at resolutions of $1.8''$ and $3.6''$ respectively. Both CO and HCN are abundant in the nucleus, where we detect two strong, curved shock fronts curling around a possible nuclear ring. The ring is clumpy and may be elongated along the bar. The kinematics of the gas can be fit with a model with infall motions up to 100 $\mathrm{km\,s^{-1}}$ along the shocks and quasi-circular rotation in the ring. We estimate the radii of the two inner Lindblad resonances that correspond to the boundaries of the ring and to the location of shock fronts to be 0.1 and 1.2 kpc. Maximum HCN emission seems to arise at the connections of the shock fronts to the nuclear ring, at a radius of 0.6 kpc from the center of the galaxy.

Key words: galaxies: structure – galaxies: individual (NGC 1530) – galaxies: ISM – galaxies: kinematics and dynamics – galaxies: nuclei – radio lines: galaxies

1. Introduction

NGC 1530 is a SBb galaxy with a large and strong bar and two wide open spiral arms. This CO bright galaxy is an ideal subject for the study of the dynamics of molecular gas in barred galaxies. Moreover, its high declination is favorable for study by interferometers, giving almost circular tracks in the uv plane. Molecular gas is very abundant in its center, which contains $6\,10^9\ M_\odot$ of H_2 (Downes et al. 1996). The central molecular hydrogen mass is more than 25% the total mass of gaseous hydrogen in this galaxy (M(HI) + M(H_2) $\simeq\ 2.2\,10^{10}\ M_\odot$). Thus the strong barred perturbation of the potential seems to have drained toward the center a large fraction of the interstellar gas of NGC 1530.

Two straight dust lanes are visible along the bar of NGC 1530, which are signatures of shocks in the flow of molecular gas (Athanassoula 1992). Near-IR and CO(1–0) observations by Regan et al. (1995) with a resolution of $3''$ show a good correlation of dust extinction with the CO emission along the bar. These shocks compress the gas and the magnetic field, thus increasing the synchrotron emission of relativistic particles which are probably the source of the continuum emission mapped along the bar at 1.4 GHz by Condon et al. (1996). From position-velocity diagrams, Downes et al. (1996) show the alignment of gas orbits along the bar predicted by numerical simulations of gas streamlines in a barred potential. The nuclear ring and the shock fronts at the inner Lindblad resonance (ILR) were detected but still not resolved with their $3.7''$ beam. We now present higher-resolution CO(1–0) observations that confirm these results, and show better the links between the kinematics of the gas, the positions of the ILRs and the location of the shocks and the nuclear ring. We also present HCN(1–0) maps that show the distribution of the dense molecular gas, traced by HCN(1–0), relative to the more diffuse molecular gas traced by CO(1–0).

Send offprint requests to: D. Downes

2. Observations in CO(1–0) and HCN(1–0)

The observations were made with the IRAM interferometer on Plateau de Bure, France, with four 15m antennas (Guilloteau et al. 1992).

2.1. CO(1–0) data

For CO(1–0) emission, five different configurations were used, giving 30 baselines from 20m to 290m. The shorter baseline configurations were used to map a mosaic of five fields along the bar, and the observations were presented by Downes et al. (1996). In this paper, we report on the higher resolution data, which were obtained in the central field only. The antennas were equipped with SIS receivers with noise temperatures of 80 K at 114 GHz. We used the quasar 0212+735 for phase and amplitude calibration. The flux of 0212+735 was found to be constant in time (1.0 ± 0.2 Jy at 114 GHz) from comparisons with strong quasars (3C273, 3C454.3, 1749+096). We Fourier transformed the visibilities with natural weighting and restored the data with the CLEAN algorithm of Clark (1980). We obtained CO(1–0) maps of the central region of NGC 1530, with a synthesized beam of $1.9''\times1.7''$ at p.a. $-74°$. In the clean beam, 1 Jy corresponds to 29 K (T_b). The resolution in velocity was 1.6 $\mathrm{km\,s^{-1}}$, which we smoothed to 20 $\mathrm{km\,s^{-1}}$ for better sensitivity. The r.m.s. noise is 6 $\mathrm{mJy\,beam^{-1}}$ in 20 $\mathrm{km\,s^{-1}}$ wide

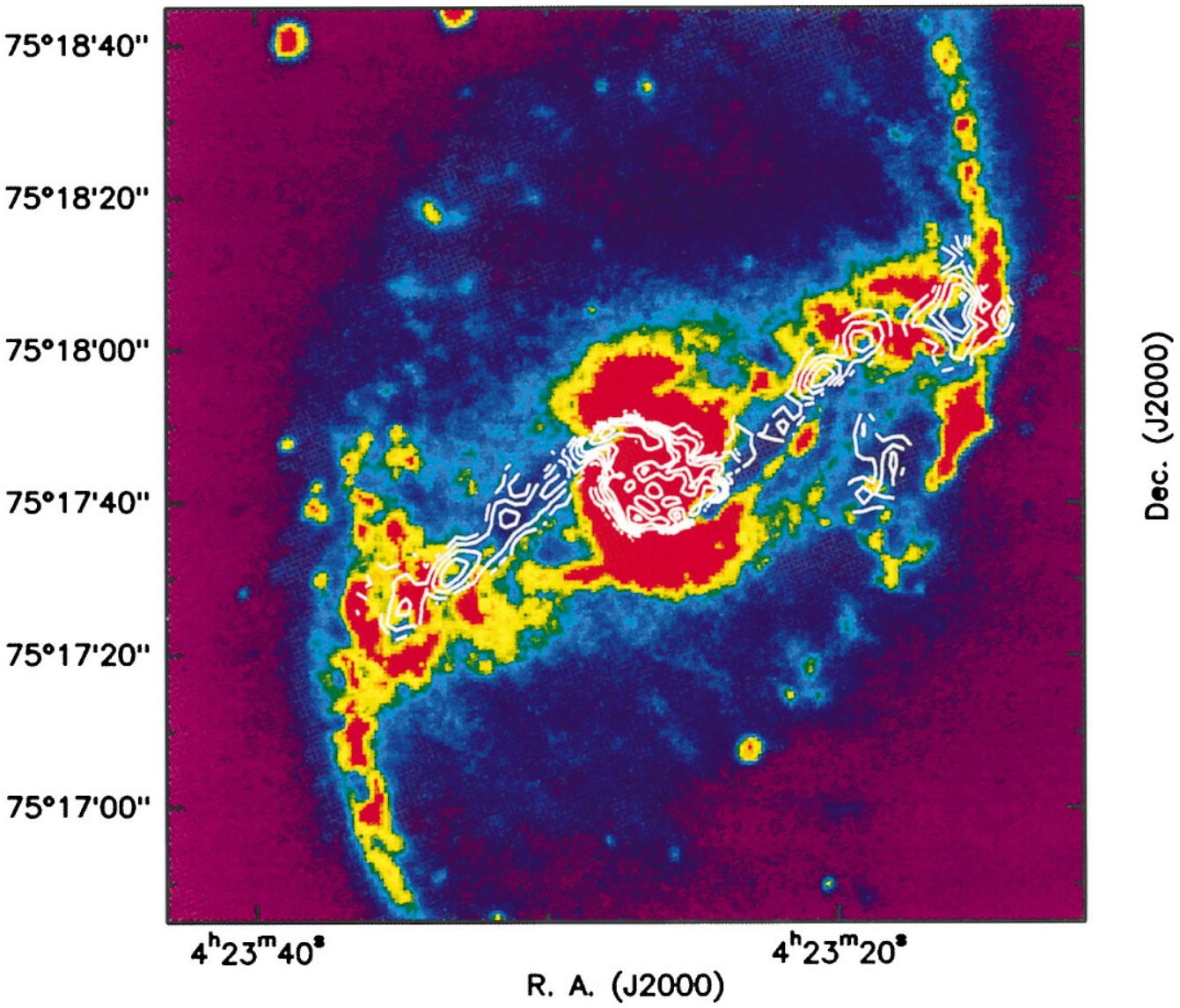

Fig. Plate 1. Superposition of *i)* CO(1–0) emission in the central plateau integrated over 540 km s^{-1} (1.8″ resolution), from Fig. 1; *ii)* CO(1–0) emission along the dust lanes, outside of the center, integrated over 120 km s^{-1} (3.7″ resolution, from Downes et al. (1996)) and *iii)* optical image (Kitt Peak 4m telescope, copyright National Optical Astronomy Observatory). *i)* and *ii)* are in white contours, *iii)* is in false color, with the maximum brightness in red and the minimum in blue. Note the good correlation between the dust lanes (blue) and the CO emission up to the ends of the bar.

channels void of line emission. To produce integrated intensity maps and intensity-weighted velocity maps, we computed the moments with a 2σ (12 mJy beam^{-1}) signal threshold. In this paper, all velocities are relative to the local standard of rest (lsr) corrected for the standard solar motion. To obtain heliocentric velocities, subtract 5.7 km s^{-1}.

2.2. HCN(1–0) data

The HCN(1–0) observations at 87.9 GHz were performed at the IRAM interferometer with 24 baselines ranging from 25m to 250m. We used the same methods for data acquisition, data reduction and map making as for the CO(1–0) transition. We assumed a flux of 1.4 Jy for the calibrator 0212+735 at 87.9 GHz. We obtained 20 km s^{-1} wide channel maps in the HCN line, with a synthesized beam of 4″×3.1″ at p.a. 66°. In the clean beam, 1 Jy corresponds to 12.8 K (T_b). The r.m.s. noise is 2.5 mJy beam^{-1} in 20 km s^{-1} wide channels void of line emission, which allowed computation of moments with a 2σ (5 mJy beam^{-1}) threshold.

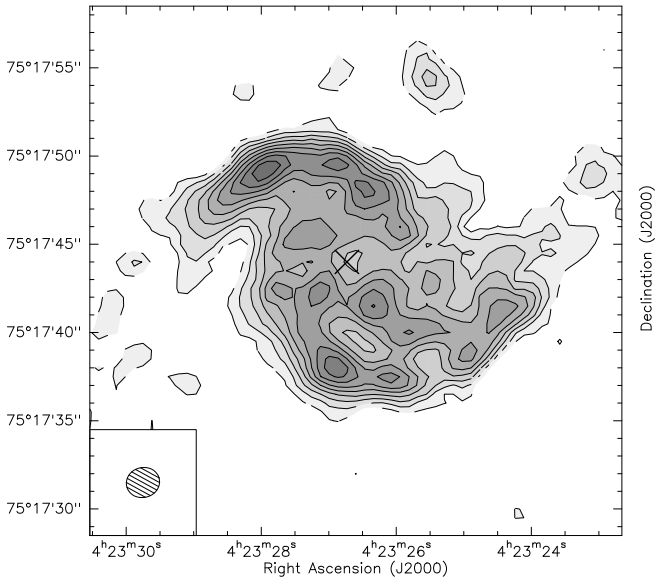

Fig. 1. Map of the integrated CO(1–0) intensity of the center of NGC 1530. The velocity range for integration is [2190 km s^{-1}, 2730 km s^{-1}]. The interval is 1 Jy beam^{-1} km s^{-1} starting at 1 Jy beam^{-1} km s^{-1} ($\simeq 2\sigma$). The cross indicates the position of the dynamical center (α = 04$^{\rm h}$23$^{\rm m}$26.73$^{\rm s}$, δ = 75°17′44.0″ ; J2000). The 1.9″×1.7″ clean beam is indicated at lower left.

3. Results

3.1. Detailed CO emission

Fig. 1 shows our new map of the integrated CO(1–0) emission in the inner 5.4 kpc (30″) of the galaxy NGC 1530, not corrected for attenuation by the 43″ primary beam. Only the "central plateau" in the maps of Downes et al. (1996) and its close connections to the CO lanes along the bar were mapped here. The data shown in Downes et al. (1996) covered the entire bar, with a beam twice as large (3.7″) as the beam of Fig. 1. To illustrate the difference between our previous low-resolution mosaics and the new high-resolution maps of the central region, we present in Plate 1 an overlay of three images: *i)* a CO(1–0) mosaic of five fields along the bar at 3.7″ resolution integrated over velocity channels which have emission from the CO lanes (120 km s^{-1} wide around 2460 km s^{-1}); *ii)* the high resolution (1.8″) CO(1–0) map of the central region of NGC 1530, integrated over 540 km s^{-1} from Fig. 1; and *iii)* an optical image of the galaxy. Note that the CO emission is regularly distributed (the distribution is smoother for the eastern side of the bar) all along the dust lanes on each side of the bar. The image of Plate 1 can be compared with Fig. 2 of Regan et al. (1995). They present a map of total intensity CO(1–0) of NGC 1530 made with the Berkeley-Illinois-Maryland Array (BIMA) at a similar resolution ($\simeq$ 4.8″) but with lower sensitivity due to smaller dishes and higher receiver noise. The extended CO lanes are distorted and marginally detected with BIMA, which explains the difference between the maps of the BIMA and the IRAM interferometers.

The individual 20 km s^{-1} wide channel maps are shown in Fig. 2, for velocities ranging from 2290 to 2650 km s^{-1}(lsr). Only maps with significant emission are shown. At a distance of 37 Mpc for NGC 1530 (Tully 1988), 1″ = 179 pc along the major axis of the galaxy.

The molecular gas has the following distribution:

– *Two narrow and bright arcs* limiting the molecular plateau, symmetrically disposed north and south with respect to the dynamical center of the galaxy, (marked with a cross in Fig. 1). These arcs have a very regular curved shape, with the concave side turned towards the bar major axis. The apparent curvature is more extreme than the real curvature because of the galaxy's high inclination (55°; Grosbol 1985). These arcs recall the curved end of dust lanes along the leading side of the bar in barred spiral galaxies, such as NGC 1433 (Athanassoula 1992). The interferometer beam fully resolves the arcs along the bar axis, while the arcs are only marginally resolved perpendicular to the bar. The length of the arcs is about 4.0 kpc (corrected for projection) while the width is about 400 pc after deconvolution for a gaussian shape. Channel maps containing emission from these arcs have lsr velocities from 2290 km s^{-1} to 2410 km s^{-1} and 2550 km s^{-1} to 2650 km s^{-1}.

– *A marginally resolved nuclear ring, or nuclear spiral*, surrounding a central cavity. This nuclear feature appears to be slightly inside the two arcs and possibly connected to them. The central cavity is coincident with the dynamical center. The cavity diameter is 3″, which gives a deconvolved radius of 210 pc. This nuclear feature contains three major clumps. If it is a ring seen in projection on the sky, the general shape of this ring is elliptical along the bar, and the major axis of the ring coincides within 20° with the minor axis of the galaxy. Its true ellipticity is even greater. The ring external radius is 3.5″ (0.6 kpc) perpendicular to the bar, and about 5″ (1.5 kpc corrected for inclination) along the bar. This gives an axial ratio of b/a = 0.4. Channel maps containing emission from this ring have velocities from 2370 to 2570 km s^{-1}.

The connections between the arcs and ring regions are revealed by two symmetric shock-like structures north and south of the nuclear ring. These shocks have heads showing strong emission linked to the ring and extended tails linked to the extremities of the arcs. They are clearly seen in individual channel maps at 2370 and 2570 km s^{-1}(Fig. 2). Figure 3 is a sketch of these arcs and ring features superposed on the CO map.

An alternative interpretation is that instead of an arc/ring system, there is only one unique large ring seen in projection as an ellipse with major axis perpendicular to the bar. This ring comprises the two arcs and the three major clumps seen inside them (see Fig.1). With an inclination of 55° for the galaxy, the shape of this large ring in the plane of the galaxy may be almost circular, with an 1.2 kpc radius. In this interpretation one can also regard the ring as unresolved arms of a central mini-spiral.

The total CO flux measured with the interferometer in the central plateau is 1.0 10^9 K km s^{-1}pc^2 which is more than 75% of the flux measured in this region with the 30m telescope (1.3 10^9 K km s^{-1}pc^2; Downes et al. 1996). This CO(1–0) flux

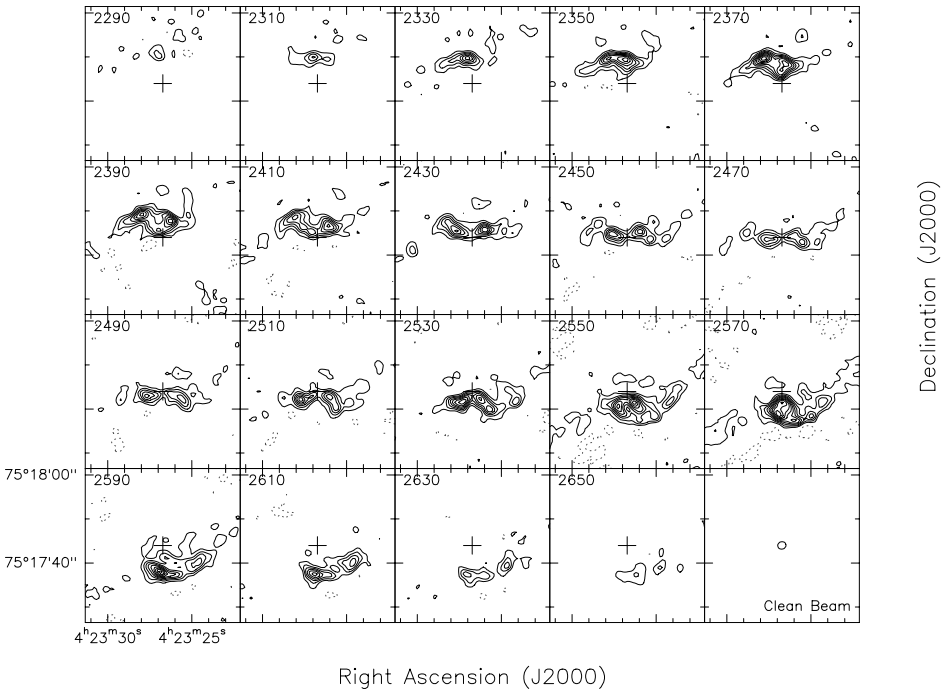

Fig. 2. CO(1–0) maps of the center of NGC 1530 in 20 km s^{-1} wide channels. Lsr velocities are indicated in the upper left corner of each channel box. The contour interval is 15 mJy beam^{-1} (2.5σ) beginning at 15 mJy beam^{-1}. The cross indicates the position of the dynamical center. The $1.9'' \times 1.7''$ clean beam is shown in the lower-right box.

of 1.3 10^9 K km s^{-1}pc^2 represents an H_2 mass of 6 10^9 $M_\odot$ for a H_2 mass to CO luminosity ratio of 4.6 $M_\odot$(K km s^{-1}pc^2)$^{-1}$. From the interferometer map corrected for primary beam attenuation, we measured the flux from the arcs on the boundary of the plateau, and found 0.47 10^9 K km s^{-1}pc^2, that is, about half the total flux. The flux of the nuclear ring is 0.32 10^9 K km s^{-1}pc^2, i.e. one third of the total flux.

3.2. The distribution of velocities

Using the 20 km s^{-1} channels, we computed the intensity-weighted velocity distribution (Fig. 4). Inside a $5''$ radius from the center, the iso-velocity contours have a regular shape, looking like the classic spider diagram with the major axis at a position angle of $\simeq 5°$, centered nearly on the dynamical center of the galaxy. This symmetry axis is indicated by the straight line across the molecular plateau in Fig. 4. This position angle is the line of nodes of the center of NGC 1530. At a radius greater than $5''$, distorsions due to the bar appear, breaking the symmetry of the isovelocity contours about the line of nodes.

The isovelocity map of Fig. 4 shows a maximum range of only $\pm$140 km s^{-1} within the region where the flux level is well above the noise, but in the individual channel maps of Fig. 2, one finds emission at 6σ from $v_{\rm lsr}$= 2290 km s^{-1} to 2650 km s^{-1} yielding a maximum line-of-sight velocity of $\pm$180 km s^{-1}. These high-velocity components along the narrow arcs indicate the location of shocks.

3.3. HCN emission

Fig. 5 shows the HCN(1–0) integrated emission and its isovelocity contours. The HCN luminosity measured from the total intensity map is 4.9 10^7 K km s^{-1} pc^2, which is somewhat more than found by single dish measurements (3.7 10^7 K km s^{-1} pc^2; Solomon, Downes and Radford, 1992). Thus the interferometer has recovered the entire HCN flux. The 20 km s^{-1} wide channel maps are shown in Fig. 6. The isovelocity contours shown in Fig. 5 are distorted by the noise in the channel maps and by velocity gradient across the beam, but the position angle for the HCN(1–0) line of nodes is about the same as for CO(1–0).

The HCN integrated intensity map has a rather complicated distribution. There are two large extended peaks disposed northeast and southwest of the dynamical center. At the center itself there is weaker HCN emission. The HCN data allow only marginal resolution of the shocks and the ring detected in CO. However, HCN seems to be emitted mainly from the inner ends of the CO arcs, at the place where they curl around to connect to the nuclear ring seen in CO. The strong emission in these two peaks amounts to 65% of the total HCN emission, whereas the two peaks amount to only 35% of the total CO emission in a CO map convolved to the same resolution as the HCN map. Further along the nuclear CO arms, the intensity of HCN emission decreases, especially for the northern arm, which is very deficient in HCN, relative to CO. The southern arm is more homogenous in HCN, but nevertheless the general trend is a decrease in the HCN emission along the arm with increasing distance from the nuclear ring. Hence the HCN seems emitted mostly at the heads of the shocks connecting the CO arms to the nuclear CO ring, at a radius of 0.6 kpc from the center of the galaxy (see sketch in Fig. 3).

To compare the CO(1–0) and HCN(1–0) maps, we smoothed the CO data to the HCN resolution and computed the ratio I(CO)/I(HCN), where I is in K km s^{-1}(Fig. 7). At this resolution the CO emission is rather uniform inside the molec-

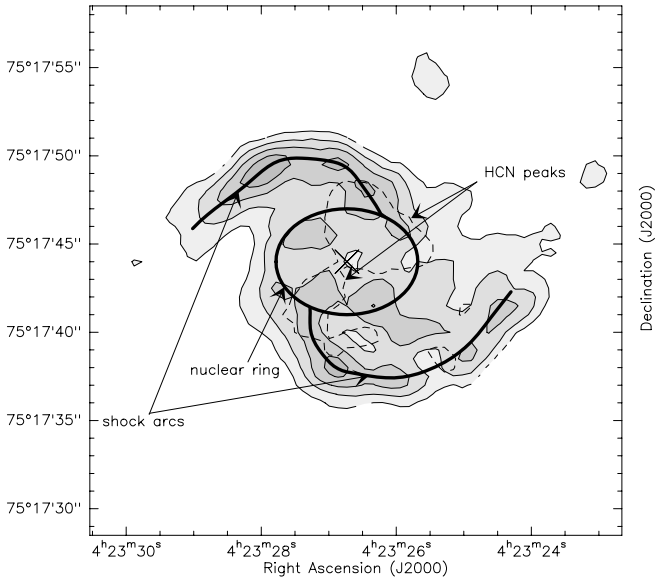

Fig. 3. Sketch of the arcs and ring features (full line) detected in the center of NGC 1530, superposed with an integrated CO map. Dashed contours show the 4σ level of HCN(1–0) emission (see Sect. 3.3).

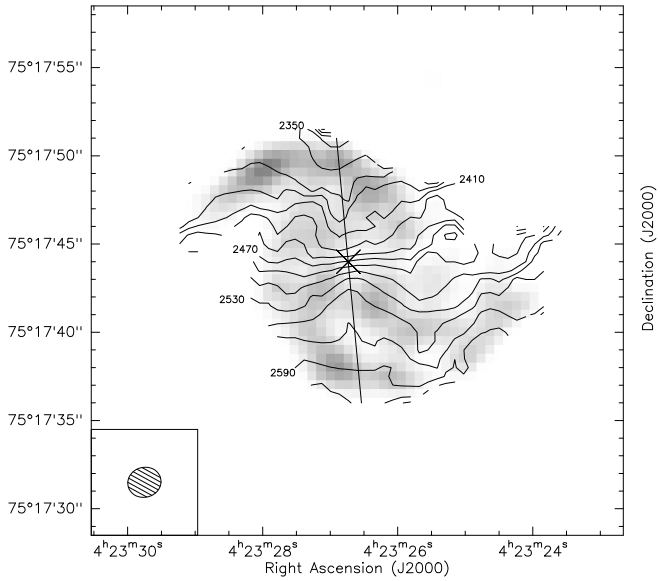

Fig. 4. Velocity field in contours of 20 $\mathrm{km\,s^{-1}}$ superimposed on the integrated CO intensity in greyscale. The lsr velocity of the dynamical center is 2472 $\mathrm{km\,s^{-1}}$. The south is redshifted, the north blueshifted. The straight line across the center is the line of nodes of the central gas distribution at PA = 5°. Labels indicate lsr velocity, in $\mathrm{km\,s^{-1}}$.

ular plateau. Hence the inhomogeneity in the ratio map is a consequence of the inhomogeneity in the HCN emission. The ratio (halftones in Fig. 7) can only be calculated where $I(\mathrm{HCN}) > 0.48$ Jy beam^{-1} km s^{-1} (2σ).

This ratio is lowest (around 7) where the HCN intensity is strongest, i.e. in the northeastern HCN peak. It is around 10 in the southwestern peak. It is generally over 14 in the nuclear arcs. The ratio exceeds 30 in the northeastern arc, where HCN is weak or absent. Thus the inner ends of the CO arcs are strongly associated with the minima of the CO/HCN ratio.

4. Analysis of the kinematics from the CO data

In this section, we discuss the kinematic features found in our data. We try to evaluate the degree of non-circular motion inside the CO disk, and to link these deviations to the presence of resonances and shocks due to the strong bar at a position angle of +115°. The study by Downes et al. (1996) had evoked the presence of an ILR at a radius of 1.5 kpc, by showing the alignment of the orbits external to the ILR with the bar. Here we examine the behaviour of the gas at the neighbourhood of this resonance and inside it. To understand the dynamics we compare the isovelocity contours with the ones expected from a model of gas flow on circular orbits. Such a model requires the knowledge of the rotation curve of NGC 1530 out to a radius of $\simeq$ 4 kpc, the limit of the CO distribution in Fig. 1.

The general symmetry of the isovelocity contours yields the position of the dynamical center (α = $04^{\mathrm{h}}23^{\mathrm{m}}26.7^{\mathrm{s}}, \delta$ = 75°17′44.0″ J2000), and the lsr systemic velocity (v_{sys}=2472 km s^{-1}). These values are consistent with those given at lower resolution by Regan et al. (1995) and Downes et al. (1996).

We assumed the galaxy is inclined by 55° to the plane of the sky. For the line of nodes Grosbol (1985) gives PA = 19° from visual inspection of the outer parts of the galaxy on optical plates, but this estimate is not precise and may be erroneous because of the bar perturbing the isophotes. This estimate may also be perturbed by a possible warp of the outer disk of NGC 1530. We assumed PA = 5° from the alignments of the isovelocity contours in the central 10″.

To get a rotation curve, we extracted the velocities along a line at PA = 5°, (see Fig. 4), corresponding to the kinematic major axis (line of nodes) of the inner 1.8 kpc (10″) of the galaxy. The line-of-sight velocity can be the circular component of the total velocity only when measured along the line of nodes. We averaged the northern ($v <$ 2472 km s^{-1}) and southern ($v >$ 2472 km s^{-1}) velocities to obtain the rotation curve of Fig. 8. Each point of the rotation curve corresponds to a radial spacing of 0.5″ (90 pc). Since the beamwidth is 1.8″ (320 pc), we actually have 10 independant measurements for the rotation curve (5 on each side).

Note the lack of symmetry of up to 30 km s^{-1} for the individual rotation curves north and south of the center, which is related to the lack of symmetry in the distribution of molecular gas in the disk and to the high dispersion of the measured velocities (the average line-of-sight velocity dispersion (FWHM) is 80 km s^{-1} in the disk). A drawback of this method of extracting velocities along the line of nodes is that we have obtained a rotation curve almost perpendicular to the bar, which is probably different from the rotation curve parallel to the bar (Athanassoula 1984). Along the nuclear spiral arms, that is, further than 5″ (0.9 kpc) from the nucleus, the rotation curve is probably per-

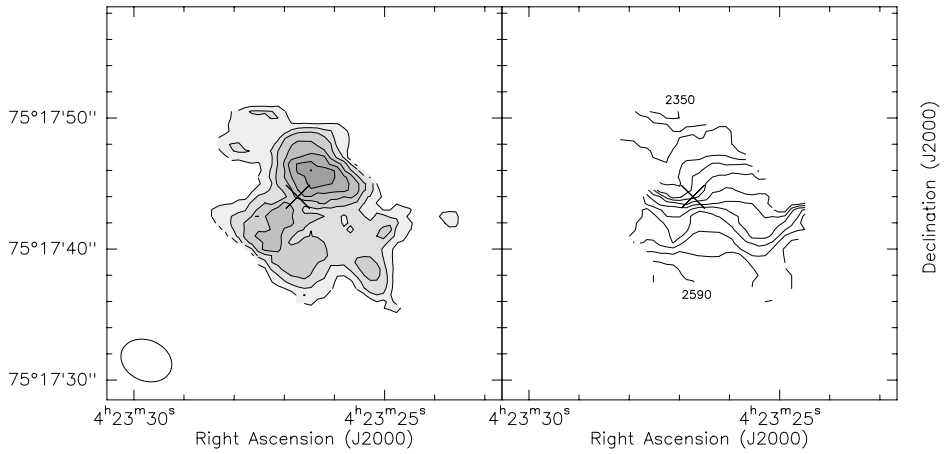

Fig. 5. (*Left*) Map of the integrated HCN(1–0) intensity in the central 30″ of NGC 1530. The velocity range for integration is [2250 km s^{-1}, 2650 km s^{-1}]. The interval of the contours is 0.24 Jy beam^{-1} km s^{-1} ($\simeq 1\sigma$), starting at 0.36 Jy beam^{-1} km s^{-1} . The 4″×3.1″ clean beam is shown in the lower left corner. (*Right*) Velocity field from the HCN(1–0) data. Labels are lsr velocities in km s^{-1}, the contour interval is 20 km s^{-1}. The cross marks the dynamical center.

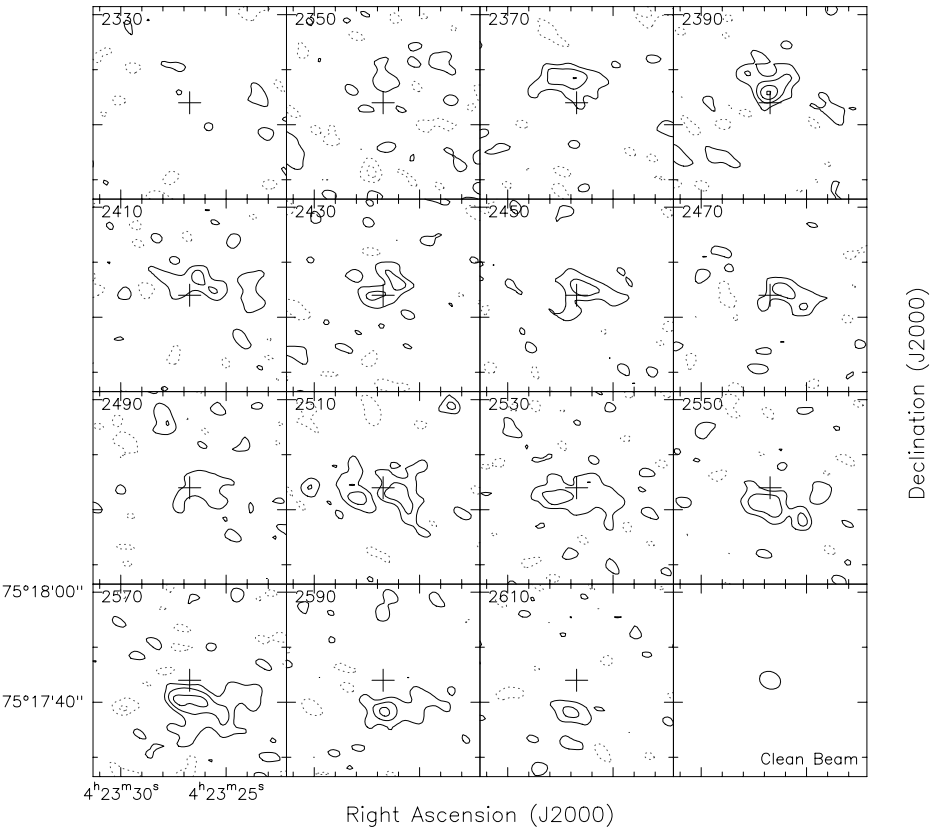

Fig. 6. HCN(1–0) maps of the center of NGC 1530 in 20 km s^{-1} wide channels. Lsr velocities are indicated in the upper-left corner of each channel box. The interval is 5 mJy beam^{-1} ($\simeq 2\sigma$) beginning at 5 mJy beam^{-1}. The cross indicates the position of the dynamical center. The 4″×3.1″ clean beam is shown in the lower right box.

turbed by a shear in the velocity distribution, due to the shocks associated with the nuclear arms.

To check our analysis we used a tilted-ring model developed by Begeman (1989) in the software package GIPSY. This program derives the kinematic parameters from the observed velocity field by fitting tilted rings to the velocity field. We binned our data in 8 rings each 1″ wide. Velocity values within each ring were weighted by the cosine of the azimuthal angle (relative to the line of nodes) in the plane of the galaxy, and we discarded all velocities within a angle of 20° around the minor axis of the galaxy. We first redetermined α, δ and $v_{\rm sys}$ by fixing the position angle of the line of nodes PA = 5° and the inclination i = 55° and varying α, δ, $v_{\rm sys}$ and the circular velocity $V(r)$ for each ring. We found the same results as above with a r.m.s. error of 0.5″ in position and 5 km s^{-1} in velocity. We then held constant α, δ and $v_{\rm sys}$ and fit for PA , i and $V(r)$. This yielded the same values as above for PA and i with an r.m.s. error of about 10° in PA and i . The values found for $V(r)$ are the same than those found in out initial analysis, with a r.m.s. error $\leq$ 5 km s^{-1}.

We modeled the rotation curve with a simple Plummer (1911) sphere for the galactic bulge plus a Toomre (1963) disk

for the galaxy's inner disk. The Plummer sphere induces a potential Φ with scale length A_b:

$$\Phi \propto \left(1 + \frac{r^2}{A_b^2}\right)^{-0.5}$$

The Toomre disk is assumed to have a surface density μ with a length scale A_d:

$$\mu \propto \left(1 + \frac{r^2}{A_d^2}\right)^{-1.5}$$

The mass of the components and their scale length were adjusted to the data. This model had four parameters (scale lengths A_b and A_d, bulge/disk mass ratio x, and total mass $M_{\rm tot}$) for five independant velocity data points. Thus the parameters were weakly constrained. We added one more condition: the maximum circular velocity induced by the potential cannot be larger than 220 km s^{-1} (for safety we slightly overestimated the maximal rotation velocity, estimated to be 170 km s^{-1} by Tully (1988)). We fixed the bulge/disk mass ratio, x, and for each value of x we determined the other parameters by least-square fits to the data.

We found from the condition of maximal velocity a lower limit for x, and an upper limit for $M_{\rm tot}$ and A_d: $x \geq 0.02$, $M_{\rm tot} \leq 6.6\,10^{10}\,M_\odot$ and $A_d \leq 2.4$ kpc. In a 2σ limit we find $x \leq 0.05$, $M_{\rm tot} \geq 3\,10^{10}\,M_\odot$ $A_b \leq 400$pc and $A_d \geq 1.7$ kpc. The minimum of χ^2 was obtained for the set of values: $x = 0.02$, $M_{\rm tot} = 6.6\,10^{10}\,M_\odot$, $A_b = 300$ pc and $A_d = 2.4$ kpc. The model with $x = 0.02$ yields the rotation curve indicated by the solid line labelled 'Bulge+Disk' in Fig. 8. The velocities induced by each component alone are also shown in Fig. 8.

We compared the observations with a data cube that would be expected from a large number of molecular clouds on circular orbits, with the rotation curve model of Fig. 8. The clouds were assumed to be randomly disposed inside a disk of 4.2 kpc radius, with the same values as the best model for i, PA, α, δ and $v_{\rm sys}$. The velocity of each cloud is simply the circular velocity at its position, corrected for projection. In this simple model, all clouds have the same mass and the same velocity dispersion ($\sigma_v = 8$ km s^{-1}), and thus contribute the same amount to the total flux. The expected flux density distribution was convolved to the angular and velocity resolution of our observations. By computing the moments of this distribution we obtained model isovelocity contours that we compared with the observed isovelocity contours. Figure 9 shows the residual velocities ($v_{\rm observed} - v_{\rm model}$). The dispersion of these residuals is 22 km s^{-1} (r.m.s.). We consider the agreement good, since the total velocity dispersion is 360 km s^{-1}. In fact, the arc and ring regions decribed in the previous section behave in radically different ways: –*Inside a circular disk* with a $\simeq$ 1.0 kpc radius (seen elliptical in projection), the kinematics can be well modeled by circular motion with the rotation curve of Fig. 8, with an extremely low r.m.s. for the residuals (10 km s^{-1}).

–*Along the bright arcs* the hypothesis of circular rotation breaks down, as one can see in the north-eastern and the south-western parts of the central plateau (Fig. 9). In both arms the difference in velocity between observations and model increases to 70 km s^{-1}, positive in the south and negative in the north.

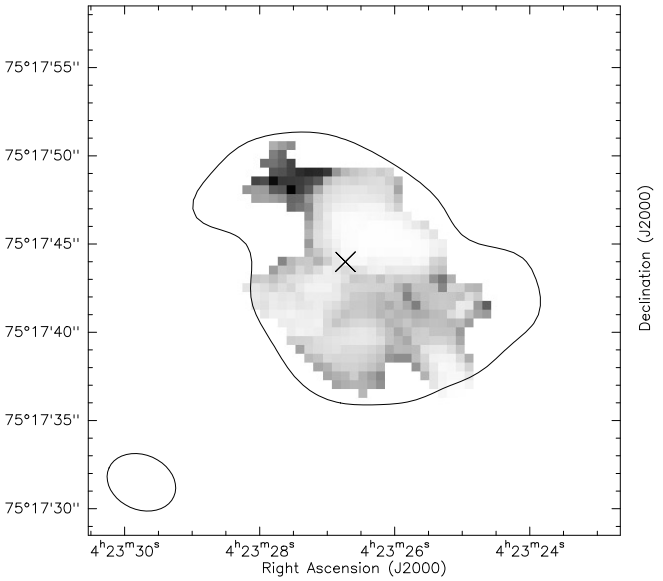

Fig. 7. Grey scale map of the ratio of integrated intensities I(CO)/I(HCN) in the central 30″ of NGC 1530. The ratio was taken only in the region where the HCN signal was $> 2\sigma$. The halftone limits are (7,34), increasing from white to black. The contour line is the 12σ ($\simeq$ 86 K km s^{-1}) level of the convolved CO distribution. Note that the HCN emission is more strongly concentrated in a few clumps than is the CO emission.

There are two ways to explain the failure of the model in the arcs. i) An underestimate of the rotation velocity, or ii) strong non-circular motions. If one tries to explain the entire phenomenon with circular motions, one needs a rotational velocity $v(\sin i \cos\phi)^{-1} = 400$ km s^{-1} ($i = 55°$, $\phi = 68°$) in the southern arc. This value is much higher than that given by Tully (1988) from HI data ($v_{\rm max} = 170$ km s^{-1}). So even with shocks it is difficult to believe that the circular motions alone are sufficient. If one supposes that the model fails because of non-circular motions in the arcs, one finds infall motions of 100 km s^{-1}. The motion is infall if the large-scale spiral structure of NGC 1530 is trailing, as is generally believed for spiral galaxies.

5. Behaviour of the molecular gas in the inner parts of NGC 1530

In models of barred galaxies, the location of resonances helps to understand the dynamics of stars and gas. The outer Lindblad resonance (OLR) is near the ends of spiral arms, the corotation radius (CR) is at or beyond the ends of the bar and the inner Lindblad resonances (ILR), when they exist, are expected near the nucleus. Numerical simulations show that a bar exerts a torque on the molecular clouds, exchanging angular momentum with them via viscous dissipation and formation of shocks. The direction of the torque on a molecular cloud depends on the

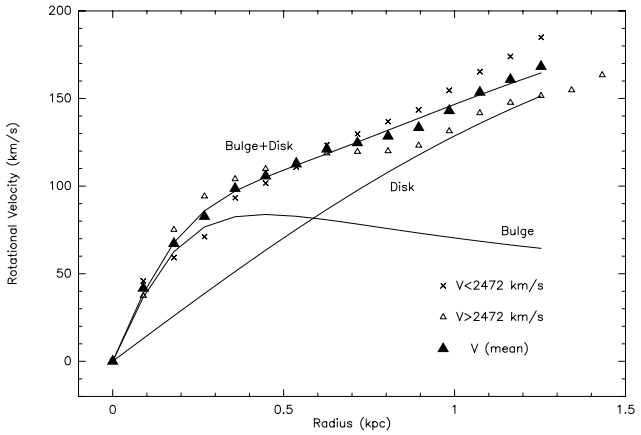

Fig. 8. Data points represent rotational velocity, measured along the line of nodes, and corrected for inclination. The crosses indicate velocities below systemic, the open triangles velocities above systemic, and the filled triangles show their mean. The three continuous curves shows the rotation curve derived from the mass model described in the text, for both components together and for each component alone.

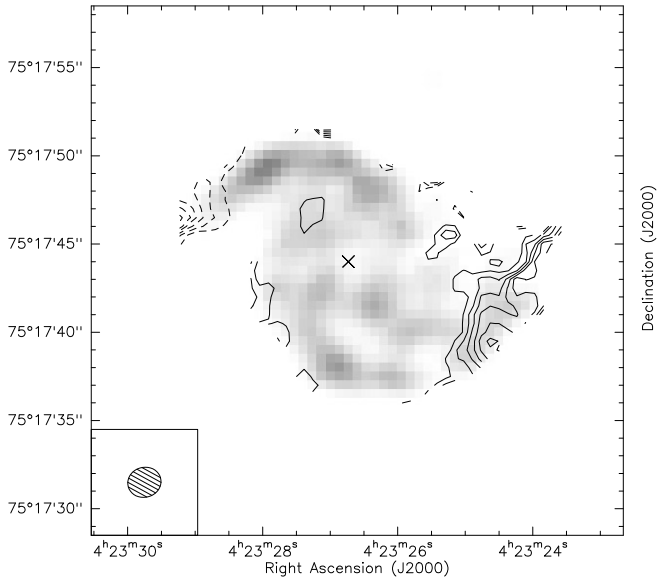

Fig. 9. Velocity residuals ($v_{\rm observed} - v_{\rm model}$) of the central regions with a model velocity field derived by fitting a Plummer sphere plus a Toomre disk model to the rotation curve. Positive residuals are in solid contours, negative residuals in dashed contours. Contour levels are $\pm 20, 30, 40, ..., 80\,{\rm km\,s^{-1}}$. The CO integrated intensity is in greyscale.

cloud's position relative to the resonances. Gas flows outwards from the CR to the OLR. From the CR to the ILR the flow is inwards. Once at the ILR, the gas is stabilised on circular orbits, and forms a ring. Gas is no longer torqued by the bar (see, e.g. Sanders & Huntley 1976; Contopoulos 1980; Athanassoula 1984; Combes & Gerin 1985; Combes 1988; Binney et al. 1991; Piner, Stone & Teuben 1995).

This torque provokes the accumulation of gas in outer rings often found at the ends of spiral arms in the disk (the location of the OLR). It accounts for the nuclear molecular ring found in many barred galaxies, like NGC 1097 (Gerin et al. 1988) or NGC 4314 (Garcia-Baretto et al. 1991; Combes et al. 1992; Benedict et al. 1996).

5.1. Finding the inner Lindblad resonances

With the kinematic model proposed in the previous section, we are able to calculate the angular velocity $\Omega(r)$, the epicyclic frequency $\kappa(r) = (4\Omega^2 + r{\rm d}\Omega^2/{\rm d}r)^{0.5}$, and to derive the location of inner Lindblad resonances (ILR) from the condition $\Omega(r_{\rm ilr}) - \Omega_p = \kappa(r_{\rm ilr})/2$, where Ω_p is the pattern speed of the bar.

We estimated Ω_p by supposing the corotation to be at the end of the bar, and the velocity of the gas at corotation to be the maximum velocity measured in the galaxy (the rotation curve is assumed to remain constant beyond its turnover point). So $\Omega_p = v_{\rm max}/r_{\rm corotation}$. Taking into account all the uncertainties, we estimate that Ω_p lies between 9 km s^{-1} kpc^{-1} and 22 km s^{-1} kpc^{-1}, so a reasonable value is $\Omega_p = 17\,{\rm km\,s^{-1}\ kpc^{-1}}$.

Fig. 10 shows the curves $\Omega(r)$, $\Omega(r) - \kappa(r)/2$ and Ω_p inside a 1.5 kpc radius from the center. The intersections of the $\Omega - \kappa/2$ curve with Ω_p gives the locations of two ILRs that are situated at radius 0.1 kpc and 1.2 kpc. The radius of the second (inner) ILR is very small and rather uncertain since the resolution of our observations (0.3 kpc) is greater than this radius. However Fig. 10 shows it is well constrained by the velocity distribution, with possible values between 0.10 and 0.15 kpc. The radius of the first (outer) ILR is not well determined, because of the flatness of $\Omega - \kappa/2$. This flatness is probably due to a slight overestimate of $\Omega - \kappa/2$ because the shear from the shocks steepens the rotation curve for radii greater than 1.0 kpc. The first ILR may be between 1.0 and 1.5 kpc.

5.2. Shocks along the bar

Inside corotation, molecular clouds move on closed elliptical orbits, denoted x_1 when elongated along the bar or x_2 when perpendicular to the bar (Contopoulos & Mertzanides 1977). Near the first ILR, the orbits change from x_1 exterior to the resonance to x_2 interior to it. Viscous dissipation forces a continuous switch between the two families of orbits, and shocks are formed due to the changing orientation of orbits, giving birth to the dust and gas lanes along the leading side of the bars of most SB galaxies. Inflow motions of the order of 100 km s^{-1} are expected along these shocks (e.g. Roberts, Huntley & van Albada 1979, Athanassoula 1992).

In the weakly barred spiral NGC 4321 (M100), trailing molecular spiral arms with a clear signature of shocks in the isovelocity contours near the first ILR were interpreted by Sakamoto et al. (1995) as gaseous orbit crowding. Recent observations of NGC 1068 which has a bar in infrared and CO (Helfer & Blitz 1995) show similar features of nuclear spiral arms.

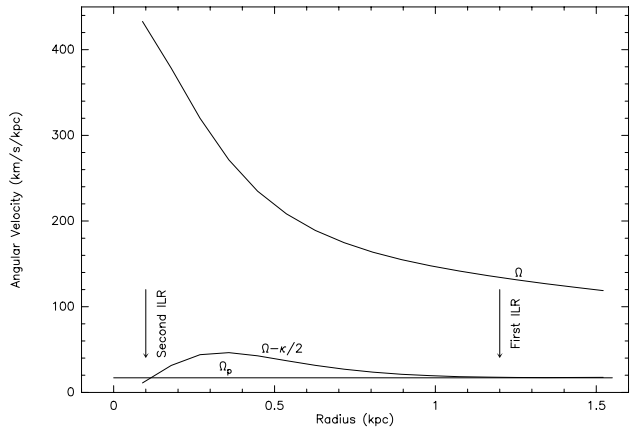

Fig. 10. Angular velocities Ω and $\Omega - \kappa/2$ derived from the CO distribution in the inner 1.5 kpc of NGC 1530. The angular velocity Ω and epicyclic frequency κ are calculated from the model of the rotation curve of Fig. 8. The horizontal line indicates the pattern speed $\Omega_p = 17\,\mathrm{km\,s^{-1}\ kpc^{-1}}$.

We think that the narrow arcs surrounding the central plateau of NGC 1530 can be interpreted in a similar manner. They leave the nucleus near the first ILR, at 1.2 kpc and vanish at $\simeq$4 kpc further along the bar as they connect to the straight CO and dust lanes which go on up to the ends of the bar (Regan et al. 1995, Downes et al. 1996). The non-circular motions are, as predicted by Roberts et al. (1979), of the order of 100 $\mathrm{km\,s^{-1}}$The southern arm appears to have a more violent shock than the northern arm, with larger non-circular motions over more extended area (see velocity residuals in Fig. 9). The integrated HCN flux in the southern arm is also much stronger than in the northern arm, which may be due to greater shock heating and/or a higher compression of gas in the southern arm (see Fig. 5).

5.3. Gas accumulation in the nuclear ring

The possible ring detected in our CO map (see sketch of Fig. 3) has an inner radius of about 0.2 kpc, i.e. it extends inward almost as far as the second (inner) ILR. If measured perpendicular to the bar, its outer radius (0.6 kpc) is probably half of the first (outer) ILR (1.2 kpc). The ring is clumpy, with at least three compact components. The most striking characteristic of this ring is its strong elongation along the bar, with a deprojected axial ratio of 0.4. Near-IR observations presented by Regan et al. (1995) show dust in a nuclear ring, but the resolution is not sufficient to see the detailed shape of the dust ring.

Such an elongated nuclear ring has not been previously observed by millimeter interferometry. Hydrodynamic models with high resolution (2 pc within 100 pc from the center) do predict the formation of an intense nuclear ring between the two ILR (Piner, Stone & Teuben 1995), but it is circular in these models. Wada & Habe (1992) used an Smooth Particle Hydrodynamic code including self-gravity to show that an elongated ring with axial ratio around 0.3 aligned along the bar can form inside the first ILR if two ILRs are present. Combes & Gerin (1985) have shown at lower resolution (300 pc) by simulations of an ensemble of colliding clouds that an elongated gas ring can form near the locations of the ILR. Such a ring may fragment into clumps and then contract into a dense central core, depending on the fraction of gas mass to total mass (Wada & Habe 1992). Elmegreen (1994) proposed as a criterion for the stability of clumps in a gaseous nuclear ring the value of the ratio of the gas density to a critical gas density defined by $\rho_{\rm crit} = 0.6\kappa^2/G$, where κ is the epicyclic frequency and G is the gravitational constant. If $\rho/\rho_{\rm crit} > 1$, the ring is unstable against rapid axisymmetric collapse into several dense clumps, and forms a ring of "hot spots" of HII regions. The molecular ring is then eventually destroyed by the young massive ionizing stars. This scenario has been proposed for NGC 4314 (Combes et al. 1992) and its radio continuum ring, which could be external to the molecular ring. In the weakly barred galaxy NGC 4321, according to Sakamoto et al. (1995), the self-gravity of the molecular ring has already led to contraction to a compact molecular core of diameter 250 pc.

In NGC 1530, we calculate from our rotation curve that at 0.4 kpc (middle of the ring) the epicyclic frequency κ = 416 $\mathrm{km\,s^{-1}kpc^{-1}}$ and hence $n_{\rm crit}$ = 490 H_2 molecules $\mathrm{cm^{-3}}$. The peak integrated CO(1–0) flux density in the ring is $\int T_{\rm b}\,dv$ = 232 K $\mathrm{km\,s^{-1}}$. If one supposes a disk vertical scale height of 100 pc, and a conversion factor from integrated CO brightness temperature to H_2 column density $X = 3\,10^{20}$ H_2 molecule $\mathrm{cm^{-2}(K\ km\,s^{-1})^{-1}}$, then the H_2 gas density is 227 $\mathrm{cm^{-3}}$. Thus the gas traced by CO(1–0) has $\rho/\rho_{\rm crit} < 1$, and does not attain the critical density for a gravitational contraction. This is consistent with the idea that CO(1–0) traces the diffuse intercloud medium, with a typical density of $10^2 - 10^3$ H_2 molecule $\mathrm{cm^{-3}}$.

There is nevertheless dense gas, and our map in HCN(1-0) indicates that most of the HCN flux, and presumably most of the dense gas, is in the heads of the shocks connecting the CO arms to the nuclear ring, inside a radius of $\simeq$ 1.0 kpc. There is little HCN flux from the elongated components (the shock arcs), where the ratio CO/HCN is very high. These values for the ratio CO/HCN are close to the ones measured in the center of the spiral IC 342 (Downes et al. 1992). The galaxy IC 342 also shows extended CO ridges along the bar and discrete clouds at the end of these ridges where they curl around the center of the galaxy, as in NGC 1530. In IC 342, the ratio CO/HCN is 7 in the clouds, and $\geq$ 20 along the extended ridges. This might indicate large amounts of dense molecular gas ($n(H_2) \geq 10^4$ $\mathrm{cm^{-3}}$) close to the nuclear ring, and more diffuse gas along the CO ridges and arcs. Another explanation is that the temperature could vary widely in these regions of shocked molecular gas.

In summary, although NGC 1530 contains much molecular gas in both diffuse and dense states, its nuclear molecular ring may not yet have reached a sufficient density for a contraction towards the center or even for very efficient star-formation in the ring itself.

6. Conclusions

The main conclusions of this paper are:

1. The molecular gas distribution in the central 5 kpc of NGC 1530 is concentrated along arc-like shock features. A patchy molecular ring may lie inside these shock fronts.
2. Two inner Lindblad resonances could exist in this galaxy: the first ILR is at a radius of 1.2 kpc, where the shock arcs leave the nucleus. The second ILR, very close to the galactic center ($\sim$ 100 pc), may be the inner ridge of the nuclear ring.
3. The gas motion as traced by CO(1–0) is inflow external to the radius of the first ILR, and probably circular motion in the nuclear ring.
4. HCN(1–0) is almost absent along the shock arcs, except at the points where they connect to the nuclear ring. The bulk of the HCN emission arises from these two points.
5. The molecular ring seems stable against efficient star formation or against global contraction of the ring towards the center of the galaxy.

References

Athanassoula E., 1984, Physics Reports, 114, 319
Athanassoula E., 1992, MNRAS 259, 345.
Begeman K.G., 1989, A & A 223, 47.
Benedict G.F., Smith B.J., Kenney J.D.P., 1996, AJ 111, 1861
Binney J., Gerhard O.E., Stark A.A., Bally J., Uchida K.I., 1991, MNRAS 252, 210
Clark B.G., 1980, A & A 89, 377
Combes F., 1988, in Galactic and Extragalactic Star Formation, eds. R.E. Pudritz and M. Fich (Dordrecht:Kluwer) 475
Combes F., Gerin M., 1985, A & A 150, 327
Combes.F., Gerin M., Nakai N., Kawabe R., Shaw M.A., 1992, A & A259, L27
Condon J.J., Helou G., Sanders D.B., Soifer B.T., 1996, ApJS103, 81
Contopoulos G., 1980, A & A 81, 198
Contopoulos G., Mertzanides C., 1977, A & A61, 477
Downes D., Radford S.J.E., Guilloteau S., Guélin M., Greve A., Morris D., 1992, A & A 262, 424
Downes D., Reynaud D., Solomon P.M., Radford S.J.E., 1996, ApJ 461, 186
Elmegreen B.G., 1994, ApJ 425, L73
Garcia-Baretto J.A., Downes D., Combes F., Gerin M., Magri C., Carrasco L., Cruz-Gonzalez I., 1991, A & A 244, 257
Gerin M., Nakai N., Combes F., 1988, A & A 203, 44
Grosbol P. 1985, A & AS 60, 261
Guilloteau S., Delannoy J., Downes D., Greve A., Guélin M., Lucas R., Morris D., Radford S., Wink J., Cernicharo J., Forveille T., Garcia-Burillo S., Neri R., Blondel J., Perrigouard A., Plathner D., Torres M., 1992, A & A 262, 624
Kenney J.D.P., Wilson C.D., Scoville N.Z., Devereux N.A., Young J.S., 1992, ApJ 395, L79
Piner B.G., Stone J.M., Teuben P.J., 1995, ApJ 449, 508
Plummer H.C., 1911, MNRAS 71, 460
Roberts V.W., Huntley J.M., van Albada G.D., 1979, ApJ 233, 67
Sakamoto K., Okumura S., Minezaki T., Kobayashi Y., AJ 110, 1995
Sanders R.H., Huntley J.M. 1976, ApJ 209, 53
Solomon P.M., Downes D., Radford S.J.E., 1992, ApJ 387, L55
Regan M.W., Vogel S.N., Teuben P.J., 1995, ApJ 449, 576
Toomre A., 1963, ApJ 138, 385
Wada K. and Habe A., 1992, MNRAS 258, 82

This article was processed by the author using Springer-Verlag LaTeX A&A style file *L-AA* version 3.